AGU PUBLICATIONS

JGR

Journal of Geophysical Research: Oceans

RESEARCH ARTICLE

10.1002/2015JC011446

Key Points:

- Observations of the dispersion relation in landfast ice using inertial motion units
- Observed a transition from flexural-gravity waves to open water dispersion relation
- Transition period associated with up to 40% of the wave energy attenuated over one wavelength for frequencies greater than 0.15 Hz

Correspondence to:
G. Sutherland,
graigors@math.uio.no

Citation:
Sutherland, G., and J. Rabault (2016), Observations of wave dispersion and attenuation in landfast ice, *J. Geophys. Res. Oceans*, *121*, 1984–1997, doi:10.1002/2015JC011446.

Received 6 NOV 2015
Accepted 2 MAR 2016
Accepted article online 7 MAR 2016
Published online 26 MAR 2016

Observations of wave dispersion and attenuation in landfast ice

Graig Sutherland[1] and Jean Rabault[1]

[1]Department of Mathematics, University of Oslo, Oslo, Norway

Abstract Observations of wave propagation in landfast ice were obtained in Tempelfjorden, Svalbard during March 2015. Wave motion was measured near the ice edge using inertial motion units and consisted of a combination of swell from the North Atlantic and wind-generated waves. The waves were observed to be unidirectional in the ice with comparable magnitudes in the vertical and horizontal displacements. The dispersion relation was calculated from the measured phase difference between two adjacent sensors separated by a distance of approximately 60 m. Deviations from the gravity wave dispersion relation were observed during the growth phase of the waves and were consistent with the presence of flexural waves. This period of wave growth was accompanied by significant wave attenuation in the high frequency portion of the wave spectrum which persisted for 3–5 h.

1. Introduction

Surface water waves are known to have a significant impact on sea ice [*Squire et al*., 1995; *Squire*, 2007] and can break large continuous ice sheets into much smaller fragments on the order of hours [*Liu and Mollo-Christensen*, 1988; *Langhorne et al*., 1998; *Collins et al*., 2015]. While theoretical aspects of wave-ice interaction have been studied for over a century [*Greenhill*, 1886], observational evidence is relatively sparse due to the difficult and dangerous environmental conditions where sea ice is present [*Squire*, 2007].

Changing ice conditions in both the Arctic and the Antarctic have created a renewed interest in field observations of wave propagation and attenuation in sea ice [*Kohout et al*., 2014; *Meylan et al*., 2014; *Doble et al*., 2015; *Collins et al*., 2015]. These studies have primarily focused on wave attenuation [*Meylan et al*., 2014; *Doble et al*., 2015] ice break up [*Asplin et al*., 2014; *Collins et al*., 2015] and possible feedback mechanisms between surface waves and changing ice conditions [*Thomson and Rogers*, 2014]. In contrast, the study of wave propagation in sea ice, specifically observations of the dispersion relation, have remained sparse [*Squire*, 2007].

Understanding how waves propagate in sea ice requires accurate knowledge of the dispersion relation [*Liu and Mollo-Christensen*, 1988; *Squire*, 2007]. *Liu and Mollo-Christensen* [1988] attributed a rapid break up event in pack ice to a focusing of wave energy 560 km from the ice edge. They attributed the large amplitude wave that was observed to nonlinear effects, which were enhanced in ice relative to open water due to the flexural and compression terms in the dispersion relation. *Collins et al*. [2015] also investigated some nonlinear aspects of waves in ice for a coastal region and suggested a possible feedback mechanism for large waves to penetrate further distances into pack ice.

While direct observations of the dispersion relation in ice are rare, there have been a few studies which have calculated it for various sizes of ice floes. *Fox and Haskell* [2001] calculated the dispersion relation for ice floes in the Antarctic marginal ice zone, and found a similar dispersion relation to that of open water with a slight modification due to the added mass from the ice floes. The dimensions of the ice floes were an order of magnitude smaller than the dominant wavelength and no evidence of flexural motion was observed.

Using an array of three seismometers on a 1 km ice floe, *Marsan et al*. [2012] calculated the dispersion relation for infragravity waves, with a peak period between 25 and 30 s, propagating in pack ice. While no flexural motions are expected be present at this frequency, a bandpass filter was applied to separate various

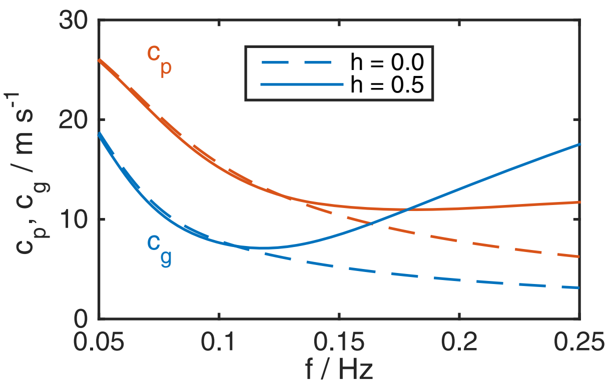

Figure 1. Phase (red) and group (blue) velocities for surface gravity waves (dashed lines) and flexural-gravity waves (solid lines) using an ice thickness of $h = 0.5$ m.

frequency components. The dispersion relation was calculated from the time shift of the correlation between adjacent sensors of the bandpass filtered signal. This required an ice thickness to give the observed group velocity that was a factor of 2 smaller than in situ measurements. The discrepancy between the measured ice thickness and that inferred from wave propagation was assumed to arise from an omnidirectional swell spectrum and *Marsan et al.* [2012] obtained a more consistent estimate of the ice thickness using an inversion technique with a variable wave direction. Since ocean swell was the dominant source for wave motion there were large errors and low correlations in the high frequency band, especially for the 0.14 and 0.25 Hz frequencies.

Presented here are observations of wave propagation near the ice-water edge in landfast ice. A brief review of some of the basic premises behind wave propagation in sea ice is presented in section 2. A description of the experimental setup and observations is presented in section 3 followed by spectral analysis of the observations in section 4. Details of the method and observations of the dispersion relation in sea ice is presented in section 5. Section 6 presents observations of wave attenuation near the edge. A discussion of the results and summary is presented in section 7.

2. Wave Propagation in Ice

There are two key components to wave propagation in sea ice: attenuation, which directly affects how the wave energy is lost, and the dispersion relation, which determines the rate of energy propagation. The two dominant mechanisms for wave attenuation in ice are due to discrete scattering from several small floes and/or inhomogeneities in the ice [*Kohout and Meylan*, 2008], or viscous effects associated with an ice continuum from frazil and grease ice [*Weber*, 1987], viscous effects in the water or ice [*Wang and Shen*, 2010] or ice creep [*Wadhams*, 1973]. Observations of attenuation have focused on lower frequency ice motion (less than 0.1 Hz) and use measurements over several kilometers to obtain accurate statistics [*Meylan et al.*, 2014; *Kohout et al.*, 2014; *Doble et al.*, 2015].

The dispersion relation for waves in sea ice is derived by modeling the ice as a thin elastic plate [*Squire et al.*, 1995]. For water of depth H, the dispersion relation relating the frequency f with the wavenumber k for an elastic plate can be written as [*Liu and Mollo-Christensen*, 1988]

$$(2\pi f)^2 = \frac{(gk + Dk^5 - Qk^3)}{\coth kH + kM} \tag{1}$$

where g is gravity, D is the bending modulus, Q is due to compression forces and M is due to the added mass of the ice sheet. The bending modulus D is a function of the rheological properties of the ice and is strongly dependent on the ice thickness, i.e., $D{=}Eh^3/\rho_w 12(1-\nu^2)$, where E is the Young's modulus, ν the Poisson ratio, h is the ice thickness and ρ_w is the water density. In general the contribution from ice compression, $Q = Ph/\rho_i$, and mass loading, $M = h\rho_i/\rho_w$, are much smaller than the gravity and flexural terms and can be neglected.

The elastic bending modulus of the sea ice cover strongly affects the dispersion relation due to the k^5 dependence and may lead to nonlinear effects even when the wave steepness ak, where a is the wave amplitude, is too small to create appreciable nonlinear effects in open water [*Liu and Mollo-Christensen*, 1988; *Collins et al.*, 2015]. Figure 1 shows the phase and group velocities calculated from (1) for open water and for an ice cover of thickness $h = 0.5$ m assuming typical rheological parameters of $E = 3 \times 10^9$ N/m^2, $P = 0$, $\rho_w = 1025$ kg/m^3, $\rho_i = 922.5$ kg/m^3 [*Squire et al.*, 1995]. Effects on the group velocity for an ice

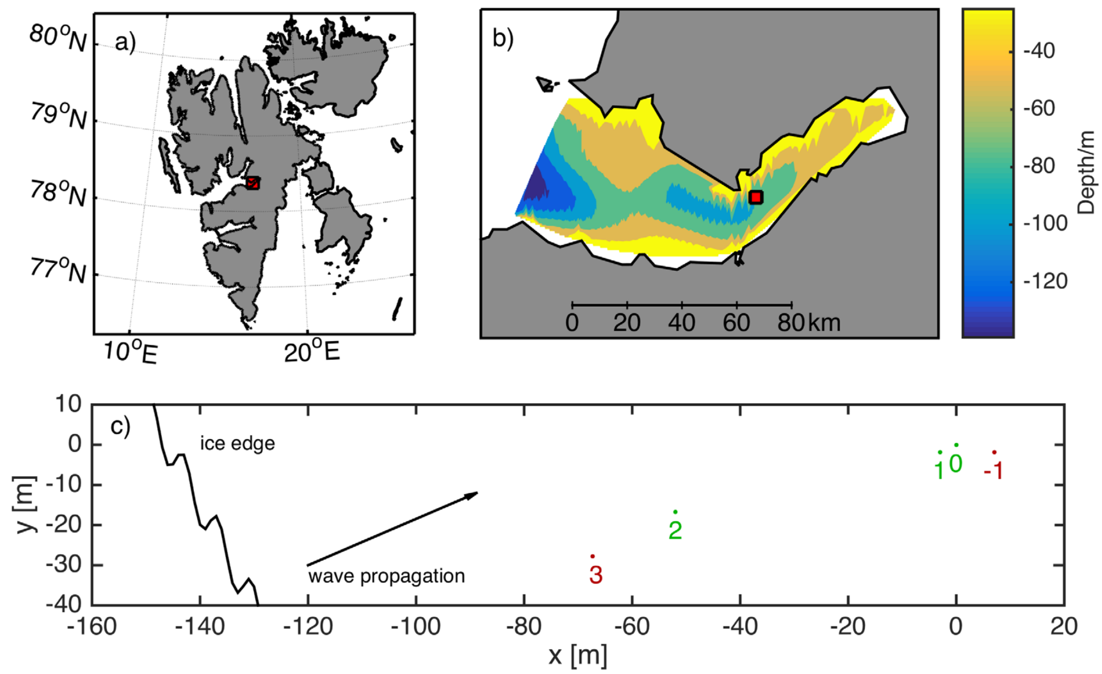

Figure 2. (a) Location of Tempelfjorden, Svalbard. The experiment site in Figures 2a and 2b is shown in red. (b) The bathymetry in Tempelfjorden. Relative sensor orientation is shown in Figure 2c along with the approximate ice edge and wave propagation direction. (c) The green points denote functioning wave sensors and the red points denote sensors that did not successfully record data.

thickness of 0.5 m can be seen in Figure 1. For frequencies greater than 0.18 Hz the group velocity (c_g) is greater than the phase velocity (c_p) with this transition to $c_g > c_p$ occurring at the local minimum of c_p.

3. Observations

Observations were made on Tempelfjorden, Svalbard between 25 March 2015 and 28 March 2015. Figure 2 shows the location of the experiment and orientation of wave sensors. The landfast ice was fastened to the shore along the edge of the fjord with the open water ice edge located approximately 100–200 m from the observation site (Figure 2c). Several inertial motion units (IMUs) and a single weather station were deployed on the sea ice. The IMUs were placed onto the ice and buried under 20–30 cm of snow. Two test holes were drilled near the measurement location, location "0" on Figure 2c, and the ice thickness was estimated from these cores to be between 0.5 and 0.6 m.

3.1. Wave Motion

The VN-100 IMU, manufactured by Vectornav Co., was used for detecting wave motion in the sea ice. Each sensor consisted of a 3-axis accelerometer, 3-axis gyroscope, 3-axis magnetometer, barometric sensor and a temperature sensor. Each IMU is factory calibrated for temperatures ranging from $-40°$ to 85°C. The accelerometer has a factory rated resolution of $5 \times 10^{-3} g$ and the angular rate resolution is 3.5×10^{-4} rad s^{-1}. The IMUs recorded the measurements at 10 Hz on a central data logger and the timestamp was synced with a GPS.

A total of 5 sensors were placed near the ice edge in Tempelfjorden, Svalbard. The sensors were deployed on 25 March 2015 16:00 until 27 March 2015 09:00. The location of each sensor, the approximate ice edge and the mean wave propagation direction are shown in Figure 2. Of the five sensors deployed, three successfully recorded data during the experiment, and are shown in green in Figure 2.

Wave displacement in the three orthogonal directions was calculated by double integrating the acceleration in each direction with respect to time. A second-order Butterworth bandpass filter was applied, with cutoff frequencies of 0.05 and 2 Hz, after each integration step to remove any low-frequency noise

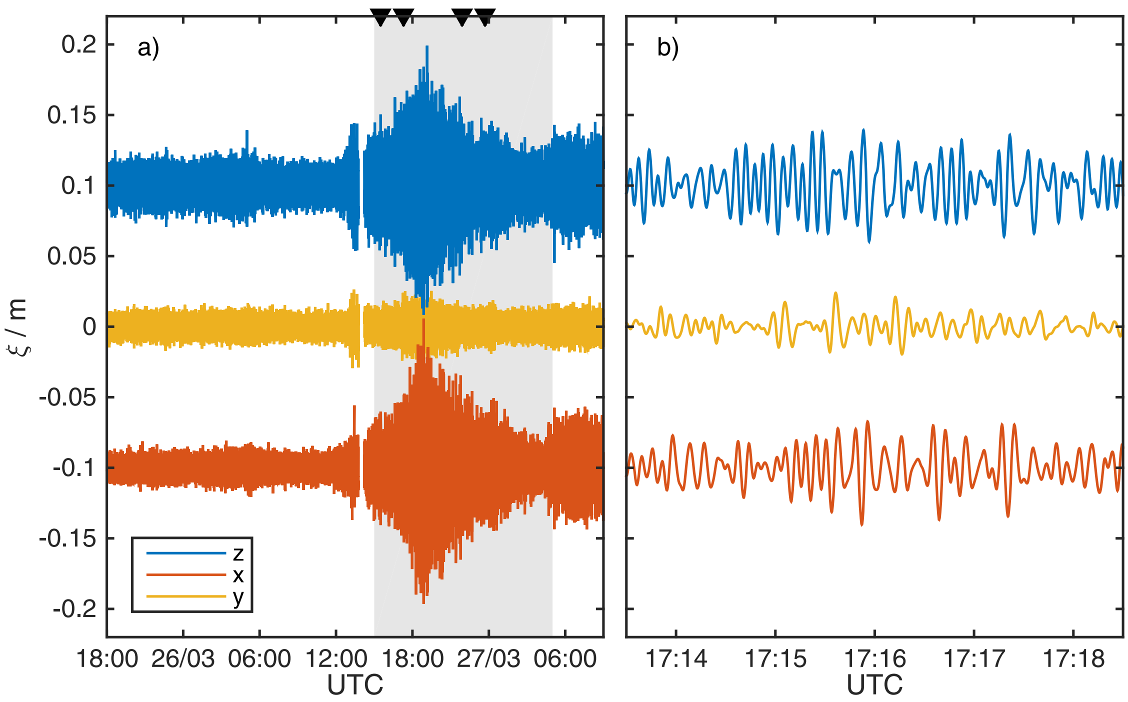

Figure 3. Time series of displacement in three directions for sensor 0. The z and x components are offset by ± 0.1 m for visualization. (a) The duration of observations with the shaded region denoting the time of wave activity used in the analysis and the black triangles denote the times for the examples in Figures 5, 6 and 7. (b) A 9 min segment centered at 26 March 2015 17:16 UTC corresponding to the second triangle to the left in Figure 3a.

associated with the integrated signal. Figure 3 shows an example time series for sensor 0 of the displacement (ξ) in the three orthogonal directions with z being the vertical and x the direction of wave propagation.

The vertical direction was determined from the gravity vector measured by the IMU as gravity was the only mean acceleration present over the duration of the experiment. This allows for the projection of the 3-axis accelerations onto this vertical vector z to obtain a true vertical motion. The horizontal direction was obtained by rotating the plane orthogonal to z to find a preferential propagation direction derived from the variance of the horizontal signal. This is compared with the magnetometer vector in the $x-y$ plane to ensure it is in the along-fjord direction. At our location, the horizontal magnetic field in the $x-y$ plane is an order of magnitude smaller than in the z direction with substantial variability on the order of hours, and thus the compass is only used to obtain the absolute mean direction over the duration of the observations. This direction is aligned with the fjord and is shown in Figure 2.

Although some wave motion was observed in the ice at 26 March 2015 12:00 UTC, we limit our analysis to the period from 26 March 2015 15:00 UTC up until 27 March 2015 05:00 (gray shaded region in Figure 3a). The 20 min gap in the data record at 26 March 2015 14:00 (Figure 3a) was due to the batteries being replaced. The observed wave motion was predominantly unidirectional with very little variance observed in the cross-fjord direction y (Figure 3).

3.2. Meteorological Conditions

Meteorological parameters such as mean wind speed, mean wind direction, air pressure, relative humidity and air temperature were measured using a Davis Vantage Pro 2 weather station mounted roughly 2 m above ice level. Ten min average values were recorded every 30 min. The meteorological conditions during the experiment are shown in Figure 4.

The wind direction in Figure 4a is aligned with the fjord so 0 corresponds to wind from the fjord to the sea and is in units of radians (positive clockwise). Before 26 March 2015 12:00 LMT the wind direction was coming from the fjord. At this time the wind shifted to the opposite direction and began to blow from the sea (Figure 4a). This shift corresponded with a rapid increase in wind speed from 1 m s^{-1} to 6 m s^{-1} over 2 h. Wave motion was observed over the time period when the wind direction was coming from the sea (shaded region, Figure 4).

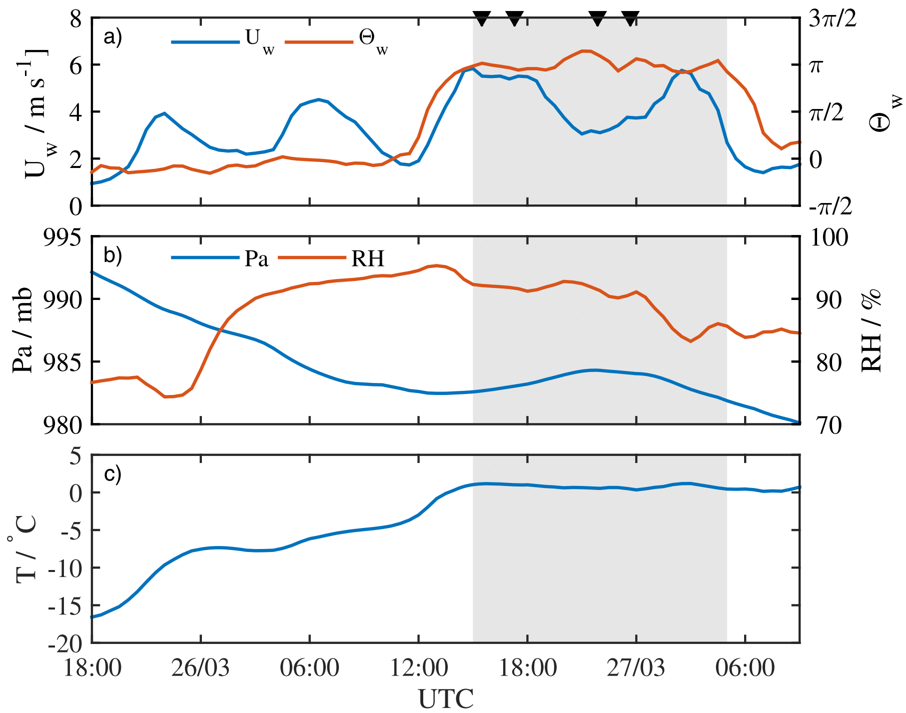

Figure 4. Meteorological observations of (a) the wind speed (U_w) and direction (Θ_w), (b) air pressure (Pa) and relative humidity (RH), and (c) air temperature (T) measured at 2 m above the ice. Θ_w is in radians and is relative to the fjord axis (positive clockwise) so 0 radians correspond to wind coming from the fjord. The shaded region shows the time period where wave motion was observed. The inverted black triangles denote the times for the examples in Figures 5, 6 and 7.

4. Wave Spectra

The power spectral density (PSD) was calculated for individual sections of 27.3 min (16,384 data points) by the Welch method [*Earle*, 1996; *Kohout et al.*, 2015]. Each section was subdivided into subsections of 2048 points with a 50% overlap and a Hanning window was applied to each subsection. The resulting PSD is the average of the Fourier transform for each subsection having 21 degrees of freedom [*Earle*, 1996]. Examples of the calculated PSD for the displacement and slope are shown in Figure 5. The units for the displacement PSD is m^2/Hz and for the slope is rad^2/Hz. The noise threshold, chosen from visual inspection to be 10 times the factory noise level, is shown by the dashed line in Figure 5. Sensitivity to the choice of noise threshold is limited to the lower frequencies due to the $(2\pi f)^{-2}$ dependence on transforming from acceleration to displacement. This sensitivity to the noise threshold will have little affect on the frequency range where flexural waves are expected to occur (Figure 1). Observations were generally greater than the noise threshold for frequencies between 0.08 and 0.25 Hz (Figure 5).

4.1. Directional Spectra

Calculating the directional spectra in sea ice is difficult for several reasons. First, the dispersion relation is a complex function of various sea ice parameters which are difficult to determine a priori. While the dispersion relation can be calculated from the PSD of the elevation and horizontal slope, this is generally used in practice to verify the response function of the wave measuring device [*Longuet-Higgins et al.*, 1963; *Earle*, 1996; *Tucker and Pitt*, 2001]. This point will be elaborated on in section 5.

To avoid the requirement of knowing the dispersion relation a priori to calculate the directional spectra, we take advantage of the fact that the wave motion in the ice was observed to be predominantly unidirectional, as can be seen in Figure 3, with comparable magnitudes in the vertical and horizontal displacements. Modeling the surface displacement as

$$\xi = \xi_z + i\xi_x, \tag{2}$$

where ξ_z and ξ_x are the vertical and horizontal displacements, allows for the calculated PSD of (2) to yield a rotary spectra where the orbital directionality can be determined.

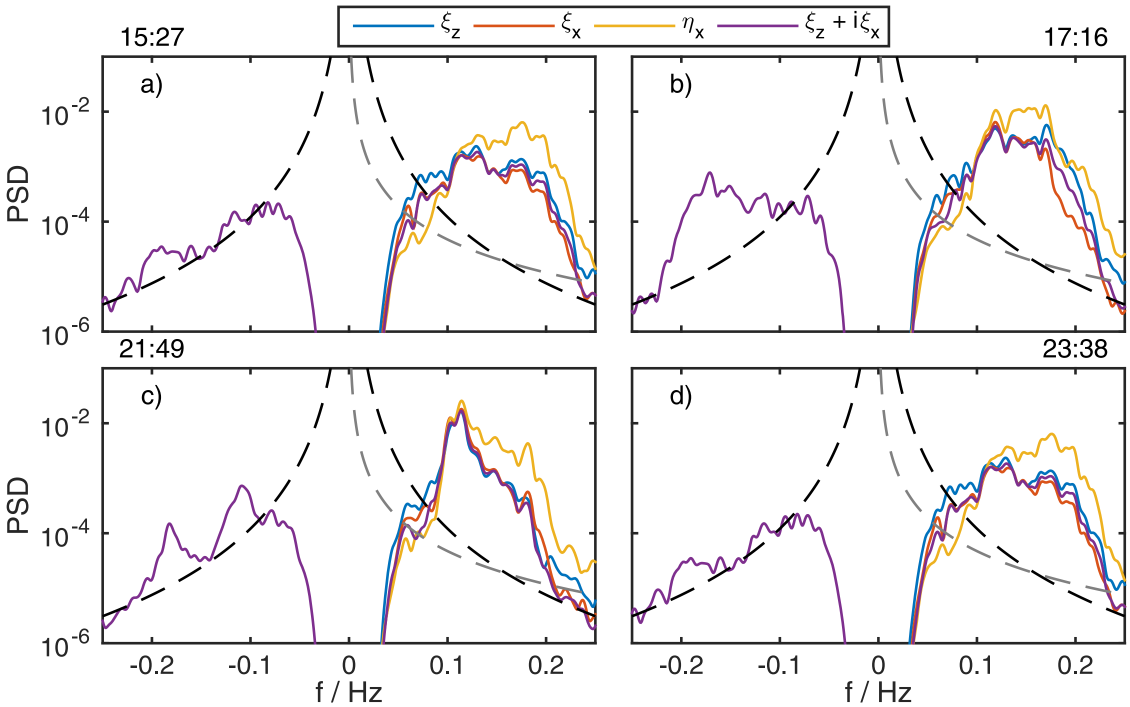

Figure 5. Power spectral density for the vertical displacement (ξ_z, blue), horizontal displacement (ξ_x, red), slope in direction of wave propagation (η_x, yellow, divided by 500 for visualization purposes) and complex displacement ($\xi_z + i\xi_x$, purple) for sensor 0 at (a) 15:27, (b) 17:16, (c) 21:49, and (d) 23:38 UTC on 26 March 2015. The blacked dashed line shows the noise level for the displacement while the gray dashed line shows the noise level for the surface slope.

Figure 5 shows the rotary PSD compared with the PSD from one dimensional measurements of the wave field. The positive frequencies denote the wave propagation into the ice and negative frequencies denote wave propagation toward the sea. The PSD was greater for waves propagating into the ice than out to sea. The PSD of (2) for positive frequencies was comparable in magnitude with the one dimensional estimates from the vertical and horizontal displacements (Figure 5). There were also appreciable peaks in the negative frequency component, especially around the time of Figure 5b, where the spectrum peak was at a higher frequency for the negative component than the positive. This will be explored further in section 6.

5. Dispersion Relation

In the absence of high resolution space and time observations to directly calculate the wavenumber and frequency, the dispersion relation can be inferred from correlating signals between adjacent sensors [*Fox and Haskell*, 2001; *Marsan et al.*, 2012] or by a single wave buoy measurement by comparing the PSD from the heave with the PSDs from the pitch and roll [*Longuet-Higgins et al.*, 1963; *Long*, 1980; *Kuik et al.*, 1988],

$$k = \frac{S_p(f) + S_r(f)}{S_h(f)} \tag{3}$$

where $S_h(f)$, $S_p(f)$ and $S_r(f)$ are the PSDs from the heave, pitch and roll respectively. In practice, (3) is not an ideal method for measuring the dispersion relation as the precise response of the measuring system, which includes the coupling of the measuring device with the media as well as the temporal response of the heave, pitch and roll sensors, must be accurately known [*Longuet-Higgins et al.*, 1963]. Often (3) is used to check the validity of the wave spectrum with the known dispersion relation [*Longuet-Higgins et al.*, 1963; *Earle*, 1996; *Tucker and Pitt*, 2001].

A more robust method to measure the dispersion relation can be calculated by looking at correlations between sensors that are relatively close to one another (preferably a distance on the order of one wavelength). The dispersion relation is calculated from the simultaneous phase difference, ϕ_{mn}, between sensors *m* and *n* separated by a horizontal displacement $\mathbf{x_{mn}}$, i.e.,

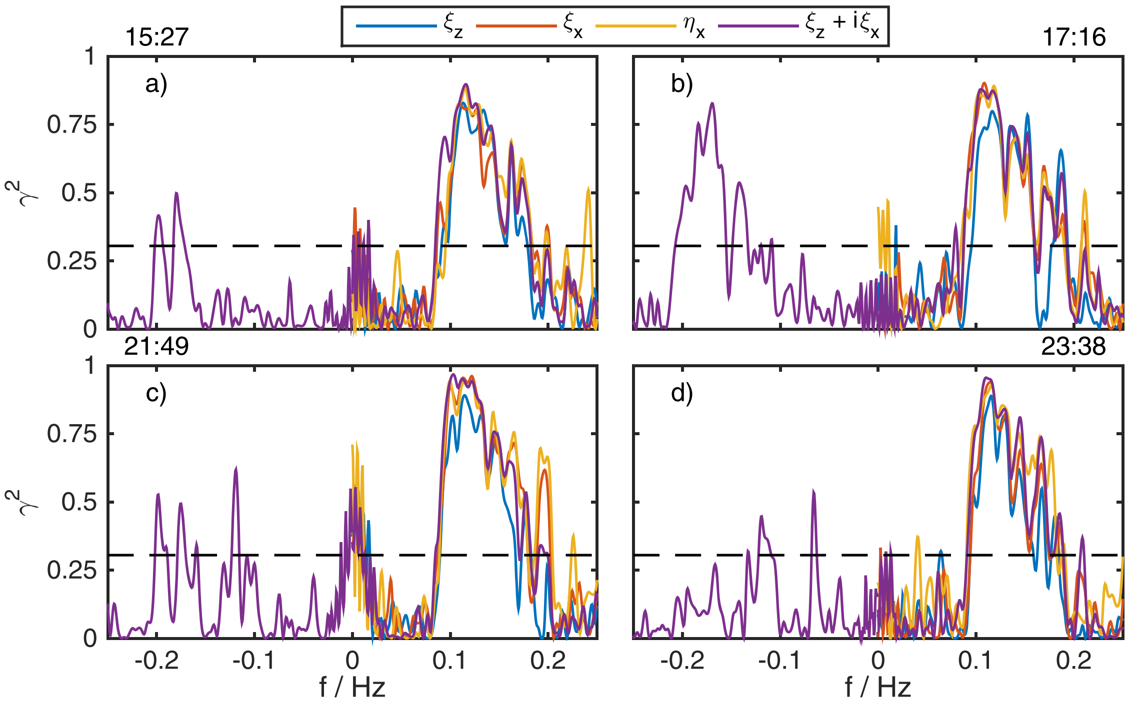

Figure 6. Spectral coherency (γ^2) between sensors 0 and 2 for the vertical displacement, horizontal displacement(ξ_x, red), slope in direction of wave propagation (η_x, yellow) and complex displacement ($\xi_z + i\xi_x$, purple) at (a) 15:27, (b) 17:16, (c) 21:49, and (d) 23:38 UTC on 26 March 2015. The horizontal dashed line denotes the coherency required to reject the null hypothesis with 99.9% confidence.

$$\phi_{mn} = \mathbf{k} \cdot \mathbf{x_{mn}} \tag{4}$$

where $\mathbf{k}$ is the vector wavenumber. There will be phase wrapping associated with wavelengths less than $|\mathbf{x}_{mn}|$, but this will be limited to no more than one phase wrap for our given sensor spacing of 60 m and a frequency range $0.1 < f < 0.25$ Hz.

To relate frequency f and wavenumber k, ϕ was calculated in the spectral domain from the cospectral density between adjacent sensors S_{mn}, i.e.,

$$\phi_{mn}(f) = \tan^{-1}\left(\frac{\mathrm{Im}[S_{mn}(f)]}{\mathrm{Re}[S_{mn}(f)]}\right). \tag{5}$$

Equation (5) was used to equate f and k assuming the signal at both locations was correlated and both were above the noise threshold. The spectral coherence (γ) between two signals was calculated with

$$\gamma^2_{mn}(f) = \frac{|S_{mn}(f)|^2}{|S_{mm}(f)||S_{nn}(f)|}. \tag{6}$$

To reject the hypothesis that the signals were not correlated at the 99.9% confidence level requires $\gamma^2 \geq 0.305$ for our PSD estimates with 21 degrees of freedom [*Amos and Koopmans*, 1963].

Figure 6 shows γ^2 for the same time intervals as Figure 5. Between 0.1 and 0.2 Hz the signal was predominantly coherent for positive frequencies. The corresponding phase shift ϕ for conditions where the coherency and signal are above their respective noise thresholds is shown in Figure 7. These were compared with the expected phase shift for the open water dispersion relation (in black) and for flexural-gravity waves (in gray) given the known distance between the sensors. There was a slight deviation from the open water dispersion for the earliest time (Figure 7a) consistent with flexural waves with an estimated ice thickness of 0.5 m. At subsequent times there is no clear evidence for flexural waves from the observed phase lag.

Figure 7 also demonstrates the relatively narrow bandwidth in which the dispersion relation from flexural-gravity waves can be differentiated from the open water dispersion relation. Equation (1) deviates from the gravity dispersion relation between the frequencies 0.11 and 0.20 Hz at which point it will cross the

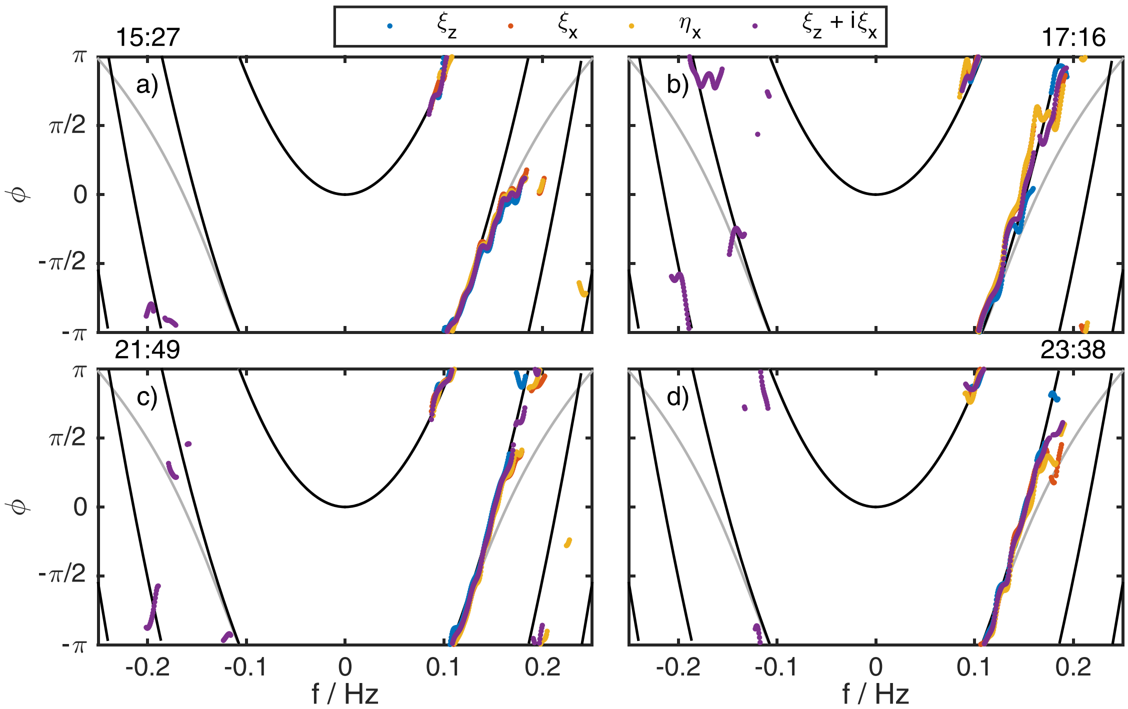

Figure 7. Phase angle between sensors 0 and 2 for the vertical displacement (ξ_z, blue), horizontal displacement (ξ_x, red), slope in direction of wave propagation (η_x, yellow) and complex displacement ($\xi_z + i\xi_x$, purple) at (a) 15:27, (b) 17:16, (c) 21:49, and (d) 23:38 UTC on 26 March 2015. The expected phase difference for open water (black) and for an 0.5 m thick ice sheet (sheet) is also shown.

wrapped phase from the gravity waves with the slower phase velocity. The difference can easily be spotted with a continuous spectrum from the slope in ϕ, but if discrete frequencies were analyzed, such as in *Marsan et al.* [2012], care must be taken to avoid ambiguities which could arise.

Figure 8 shows the calculated dispersion relation using (4) and (5) with the color denoting the time in UTC. The dispersion relation in Figure 8 was calculated using the complex height ξ to obtain the phase lag $\phi_{mn}(f)$, but there was little observed variation if the coherency of other wave signals were used. For frequencies between 0.08 and 0.12 Hz and for an ice thickness up to 0.75 m, gravity dominates the dispersion relation and the observations coincided with the open water dispersion relation (Figure 8). For frequencies

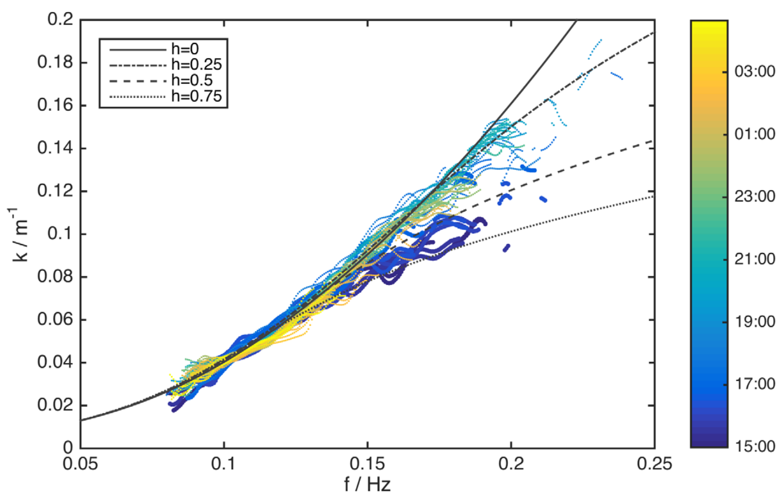

Figure 8. The dispersion relation calculated by the phase difference between sensors 2 and 0 and sensors 1 and 0. The color denotes the time of day. Times before 17:00 are denoted by slightly larger symbols. The black lines show the dispersion relation for various values of ice thickness h (solid = 0 m, dashed-dot = 0.2 m, dashed = 0.5 m, and dotted = 1 m).

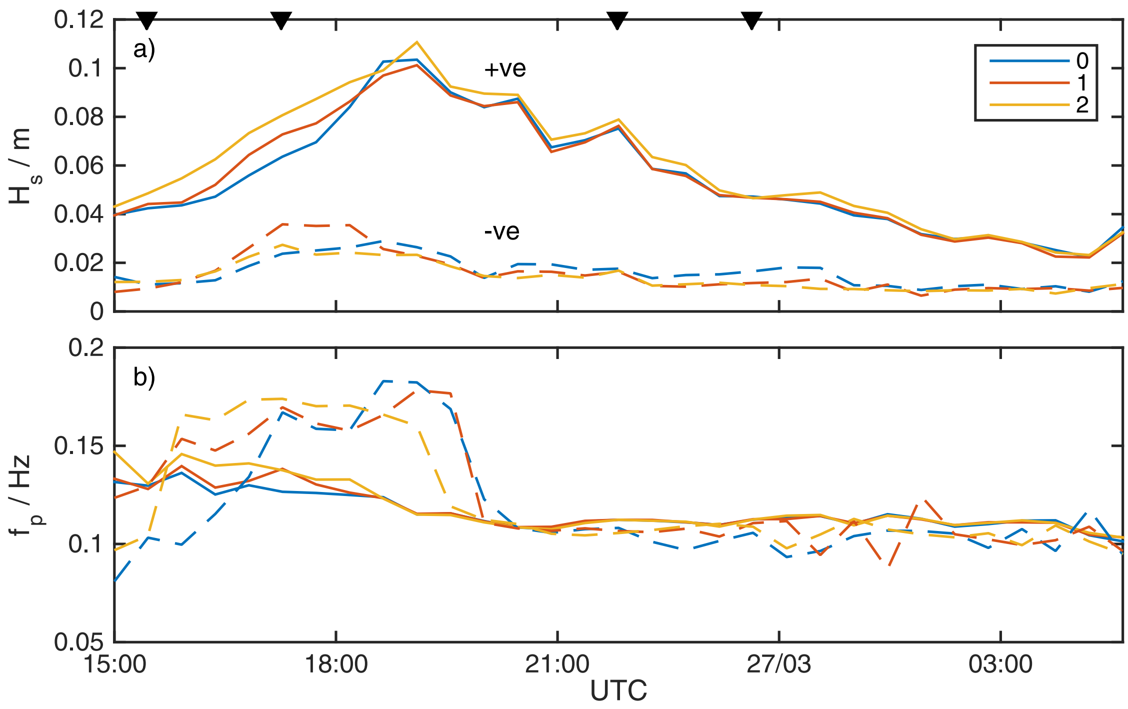

Figure 9. (a) Significant wave height and (b) peak frequency at the three sensor locations. The forward propagation in the ice (+ve) and propagation out to sea (−ve) are shown by the solid and dashed lines respectively. The inverted black triangles denote the times for the examples in Figures 5–7. The color denotes individual IMUs.

greater than 0.12 Hz there was an increasing amount of time-dependent scatter in the calculated dispersion relation. Before 17:00 UTC there was a clear deviation from the gravity wave dispersion relation corresponding to an ice thickness $0.5 < h < 0.75$ (Figure 8, heavy dots). After 17:00 UTC, this deviation vanished and the dispersion relation was similar to that of open water (Figure 8, light dots).

6. Wave Attenuation

The significant wave height H_s and peak frequency f_p are shown in Figure 9 for the three sensor locations near the ice edge. The solid lines represent wave propagating into the fjord and the dashed lines represent propagation out of the fjord. There was a clear gradient in H_s between the three sensors from 15:00 to 19:00 where the significant wave height was increasing. This time frame corresponded to a small peak in the reflected H_s (dashed line Figure 9a) and f_p (dashed line Figure 9b) suggesting that there might exist a relatively high amount of reflected energy in the higher frequency portion of the wave spectrum.

Figure 10 shows the spectrogram for the ratio of the PSD calculated at (a) sensor location 0 and 2 and (b) 1 and 2. In Figure 10, no decrease in energy corresponds to a value 0 and a 100% reduction corresponds to a value of 1. Wave attenuation was predominantly small except for the time period between 15:00 and 20:00 where as much as 80% of the energy was attenuated for frequencies greater than 0.15 Hz.

The mean spectral attenuation shown in Figure 10 was averaged between 15:00 and 20:00 as a function of frequency (Figure 11). A gradual increase in the spectral attenuation was observed for frequencies greater than 0.15 Hz. The attenuation increased linearly from 0% at $f = 0.15$ Hz to nearly 40% at $f = 0.23$ Hz. While wave-wave nonlinear interactions can redistribute energy in the spectrum, these effects are slow and will only accumulate over distances on the order of ten wavelengths [*Liu and Mollo-Christensen*, 1988].

A peak was also observed in the negative frequencies between 15:00 and 20:00 (Figure 9), suggesting that reflection/scattering may be involved with the wave attenuation observed at high frequencies. Although the source of the reflection in the sea ice was unknown, we can compare the spectral energy propagating into the ice with that propagating out at each sensor location. The spectrogram, at location 0, for positive and negative frequencies can be seen in Figure 12 and the peak frequency is shown by the dashed lines. The peak frequency for the positive frequencies slowly decayed over time while the peak frequency for the negative

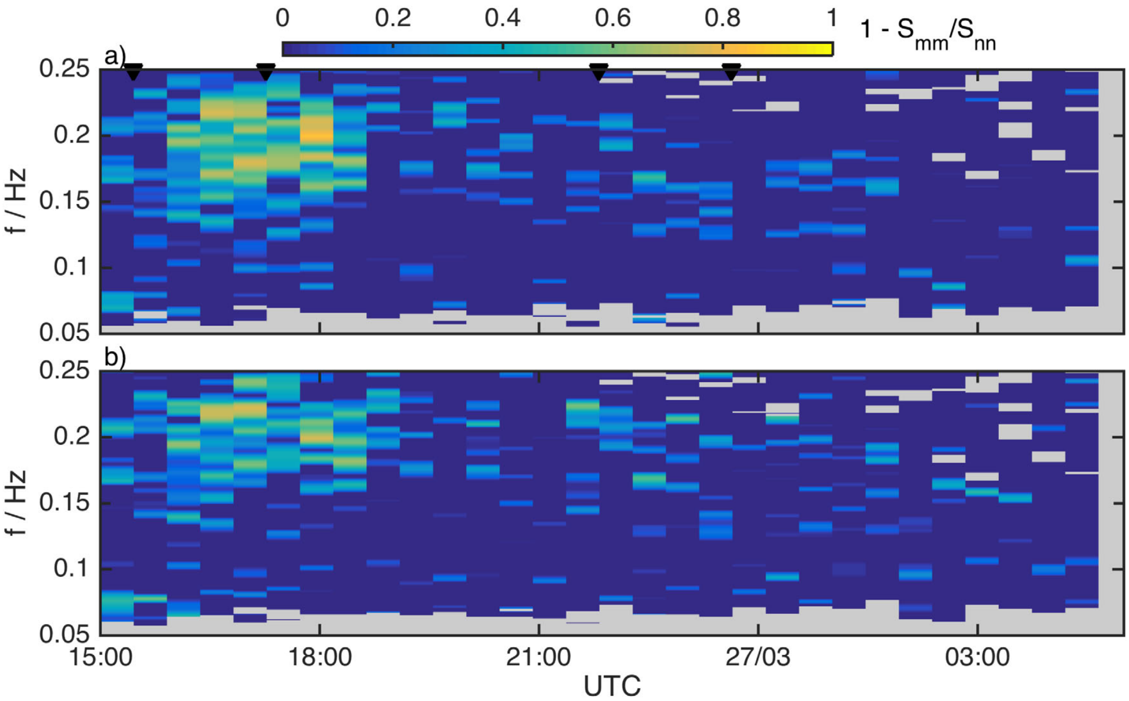

Figure 10. Spectral attenuation shown between sensors (a) 0 and 2 and (b) 1 and 2 for the forward propagating wave energy. The inverted black triangles denote the times for the examples in Figures 5–7.

frequencies was more variable (Figure 12b). Most notably was the local peak frequency for the negative frequencies between 0.15 and 0.18 Hz observed between 17:00 and 20:00 (Figure 12b). This peak in the negative frequencies was preceded by sensors 1 and 2 by 1–2 h (Figure 9b) suggesting a complex frequency dependence on the effects from ice draft and cracks which affected the wave reflection [*Squire*, 2007].

An estimate for the ratio of reflected energy is given by S_{-ve}/S_{+ve}, and is shown in Figure 13 for sensor 0. Enhanced values of S_{-ve}/S_{+ve} were observed from 17:00 in the frequency range 0.15–0.2 Hz. Although the enhancement was greatest between 17:00 and 20:00 UTC, corresponding to where the peak frequency for

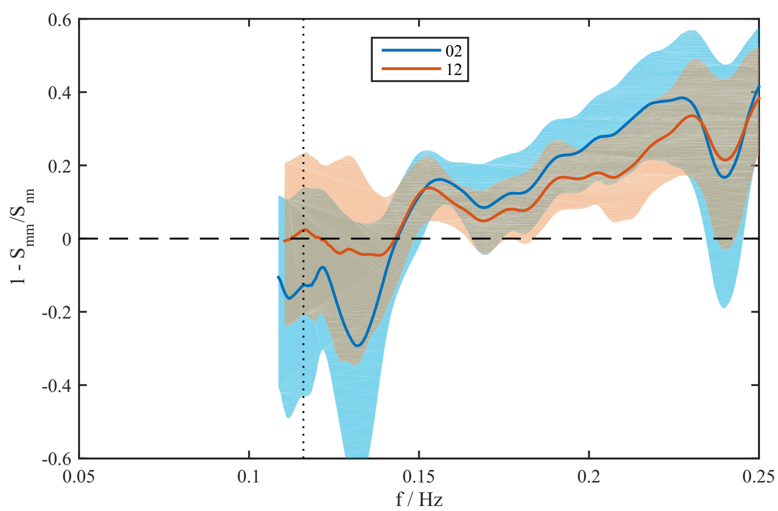

Figure 11. Mean attenuation calculated between 15:00 and 20:00 on 26 March 2015. Shaded region shows the 95% confidence interval as calculated using the bootstrap method. The vertical dotted line shows the mean peak frequency associated with incoming swell. In the legend, 02 refers to the attenuation between sensors 2 and 0, while 01 refers to the attenuation between sensors 1 and 0.

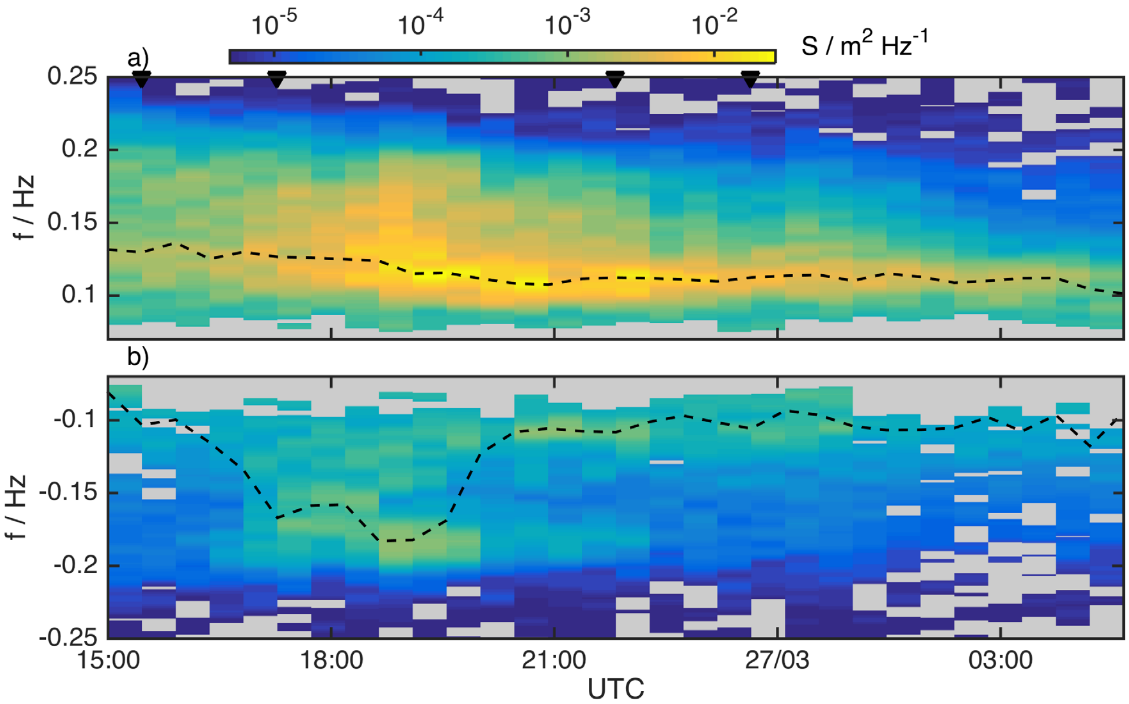

Figure 12. Power spectral density for (a) positive and (b) negative rotary components for sensor 0. The dashed line shows the peak frequency. The inverted black triangles denote the times for the examples in Figures 5–7.

the reflected wave was a maximum, the enhancement appeared to persist throughout the record for frequencies between 0.15 and 0.2 Hz when the wave motion was above the detectable limit (Figure 13).

A mean spectral reflection coefficient is calculated for the period between 15:00 and 20:00, similar to the averaging for the absolute attenuation in Figure 11, and is shown in Figure 14. This ratio estimates an "integrated reflection coefficient" for a particular sensor location as the exact location of where the reflections took place in the ice were not known. However, the location can not be too far as there is high attenuation

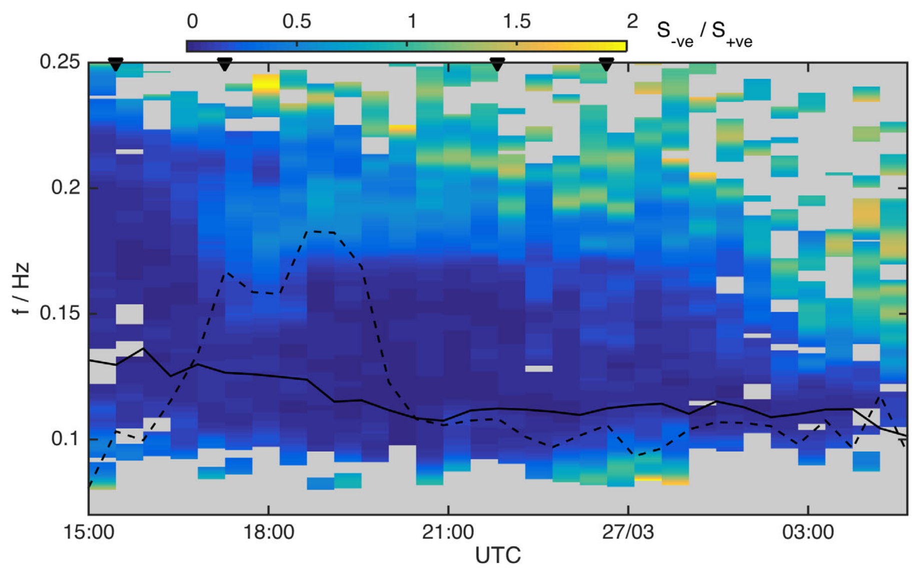

Figure 13. Ratio of negative to positive rotary spectra components at sensor 0. The solid line shows the positive peak frequency and the dashed line is the peak frequency for the negative component. The inverted black triangles denote the times for the examples in Figures 5–7.

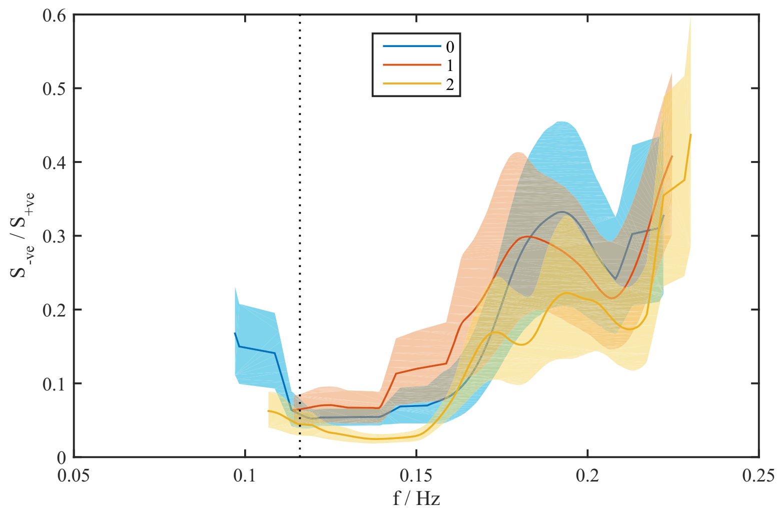

Figure 14. Mean ratio of negative to positive rotary spectra components calculated between 15:00 and 20:00 on 26 March 2015. Shaded region shows the 95% confidence interval as calculated using the bootstrap method. The vertical dotted line shows the mean peak frequency associated with incoming swell. The color denotes individual IMUs.

for frequencies greater than 0.15 Hz (Figure 11). Figure 14 has a similar structure to Figure 11 with a gradual increase in S_{-ve}/S_{+ve} for frequencies greater than 0.15 Hz.

7. Summary and Discussion

Observations of wave motion were obtained using inertial motion units near the ice-water edge in landfast ice located in Tempelfjorden, Svalbard. The dispersion relation was calculated from the spectral phase shift measured between adjacent sensors. Evidence of flexural-gravity waves, as determined from the dispersion relation, were observed during the first 2 h of the wave motion at which point there was a transition to a gravity wave dispersion relation. Cracks in the ice were not quantified, but there was a noticeable increase in their number over approximately 36 h between deployment and recovery of the sensors. These cracks appear to have an impact on the ability of the ice cover to transmit flexural stress and a shift in the dispersion relation from flexural-gravity waves to gravity waves was observed over a short period of time.

There are other possible processes, other than the presence of flexural waves, which would lead to a deviation from the open water dispersion relation as seen in Figure 8. If the medium was moving, there will be a Doppler shift and/or refraction which will depend on u/c_p where u is the velocity of the moving medium and c_p is the phase velocity. Our observations are obtained from landfast ice and u should be zero. If cracks developed and the ice moved with the local tidal currents, which are less than 0.1 m s^{-1} in this region [*Kowalik et al*., 2015], then the change in frequency will be proportional to $u/c_p \approx 0.1/10 = 0.01$ which is much smaller than the observed deviation for frequencies greater than 0.15 Hz. Wave refraction can also occur due to a change in the medium velocity, but this too shall scale with u/c_p, and our value of 0.01 is much too low for appreciable refraction [*Johnson*, 1947].

Another possible source of deviation from the open water dispersion relation comes from using (4) and the possible misalignment between $\mathbf{k}$ and $\mathbf{x_{mn}}$ for certain frequencies. For the observed deviation in Figure 8, the angle between $\mathbf{k}$ and $\mathbf{x_{mn}}$ would have to increase as a function of frequency, which seems physically implausible in the absence of refraction. It is possible that there is a complex wave pattern due to scattering of high frequency energy, but our observations are insufficient to address such spatial heterogeneity.

Appreciable attenuation in the wave spectral energy density was observed over approximately one wavelength between approximately 15:00 and 20:00 on 26 March 2015(Figure 9). The wave propagation direction was predominantly along the fjord and was separated into a positive propagating wave (i.e., into the ice) and a negative propagating component (i.e., back to sea) via a rotary spectrum of the surface

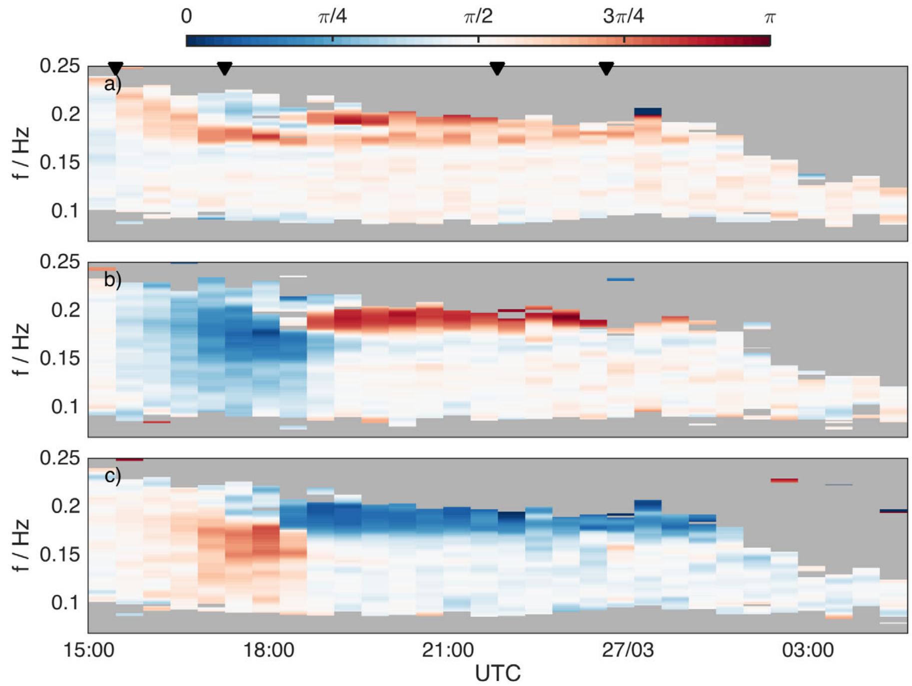

Figure 15. Phase difference between vertical and horizontal displacement for (a) sensor 2, (b) sensor 1 and (c) sensor 0. The inverted black triangles denote the times for the examples in Figures 5–7.

displacement. For frequencies less than 0.15 Hz, which was close to the frequency where the phase and group velocities are equal assuming an ice thickness of 0.5 m (Figure 1), there was no appreciable attenuation. For larger frequencies the attenuation in the power spectral density was observed to steadily increase (Figure 11). Confidence intervals are relatively large, but for frequencies around 0.2 Hz approximately 10–40% of the energy density at the outermost sensor was attenuated. The high wave attenuation occurred over the same time-spectral space where the deviation from the open water dispersion relation (Figure 8), which we suspect to be due to flexural waves, were present. The frequency dependence of the ratio of reflected to propagating wave energy (Figure 14) was very similar to that observed for the wave attenuation with similar confidence intervals for the estimates, which is consistent with scattering being the dominant process for wave attenuation in this frequency range of 0.15–0.25 Hz. A greater spatial sampling of the wave motion is required to investigate how high frequency wave energy is scattered near the ice edge.

An interesting feature of the ice motion was the comparable amplitudes in the horizontal and vertical displacements. The wave motion was expected to be primarily in the vertical [e.g., *Fox and Haskell*, 2001] and this strong horizontal motion is somewhat puzzling. It could be that cracks in the ice affected the horizontal motion or it may be that this motion is a property of wave propagation in an ice covered sea. Further experiments would be necessary to determine under what conditions horizontal and vertical motion are comparable.

The phase relation between the vertical and horizontal motion was calculated from the cospectra between the two signals. Figure 15 shows the phase difference between horizontal and vertical motions for the three sensors. For frequencies less than 0.17 Hz the phase difference was close to $\pi/2$ except for sensors 0 and 1 where the phase difference was π or 0 consistent with rectilinear motion. For all sensors at frequencies greater than 0.17 the phase was 0 or π. The time and frequencies where the wave motion was out of quadrature, i.e., $\phi \neq \pi/2$, (Figure 15) coincided with the time and frequencies where wave attenuation was the largest (Figure 11). It would be interesting to investigate whether the surface motion was related to stresses in the ice, analogous to the case of wave stresses in the ocean [*Cavaleri and Zecchetto*, 1987], as this phase shift between vertical and horizontal motions may be an important component of rapid break up of coastal sea ice.

Acknowledgments
The authors are grateful to Brian Ward at NUI Galway for providing the data logger and IMUs which made the experiment possible. We also thank Atle Jensen, Olav Gunderson, Erika Lindstrøm from UiO, Kai Christensen from met.no and Eugene Morozov from the Shirshov Institute for all their help with the field work. A special thanks to Aleksey Marchenko and the entire logistics staff at UNIS for their support on Svalbard. The authors are especially thankful to Trygve Halsne for his help in the preparation and execution of the field work. Funding for the experiment was provided by the Norwegian Research Council under the PETROMAKS2 233901 project. The data used in this study are available by request from the corresponding author at graigors@math.uio.no. The authors are grateful to the two anonymous reviewers whose comments have greatly improved the manuscript.

References

Amos, D., and L. Koopmans (1963), *Tables of the Distribution of the Coefficient of Coherence for Stationary Bivariate Gaussian Processes*, Sandia Corp., Albuquerque, N. M.

Asplin, M. G., R. Scharien, B. Else, S. Howell, D. G. Barber, T. Papakyriakou, and S. Prinsenberg (2014), Implications of fractured Arctic perennial ice cover on thermodynamic and dynamic sea ice processes, *J. Geophys. Res. Oceans*, *119*, 2327–2343, doi:10.1002/2013JC009557.

Cavaleri, L., and S. Zecchetto (1987), Reynolds stresses under wind waves, *J. Geophys. Res.*, *92*(C4), 3894–3904.

Collins, C. O., III, W. E. Rogers, A. Marchenko, and A. V. Babanin (2015), In situ measurements of an energetic wave event in the arctic marginal ice zone, *Geophys. Res. Lett.*, *42*, 1863–1870, doi:10.1002/2015GL063063.

Doble, M. J., G. D. Carolis, M. H. Meylan, J. R. Bidlot, and P. Wadhams (2015), Relating wave attenuation to pancake ice thickness, using field measurements and model results, *Geophys. Res. Lett.*, *42*, 4473–4481, doi:10.1002/2015GL063628.

Earle, M. D. (1996), Nondirectional and directional wave data analysis procedures, *NDBC Tech. Doc 96-01*, Natl. Data Buoy Cent., Natl. Oceanic and Atmos. Admin., U.S. Dep. of Commer., Washington, D. C.

Fox, C., and T. G. Haskell (2001), Ocean wave speed in the Antarctic marginal ice zone, *Ann. Glaciol.*, *33*(1), 350–354.

Greenhill, A. G. (1886), Wave motion in hydrodynamics, *Am. J. Math.*, *9*(1), 62–96.

Johnson, J. (1947), The refraction of surface waves by currents, Eos *Trans. AGU*, *28*(6), 867–874.

Kohout, A., M. Williams, S. Dean, and M. Meylan (2014), Storm-induced sea-ice breakup and the implications for ice extent, *Nature*, *509*(7502), 604–607.

Kohout, A. L., and M. H. Meylan (2008), An elastic plate model for wave attenuation and ice floe breaking in the marginal ice zone, *J. Geophys. Res.*, *113*, C09016, doi:10.1029/2007JC004434.

Kohout, A. L., B. Penrose, S. Penrose, and M. J. M. Williams (2015), A device for measuring wave-induced motion of ice floes in the Antarctic marginal ice zone, *Ann. Glaciol.*, *56*(69), 415–424.

Kowalik, Z., A. Marchenko, D. Brazhnikov, and N. Marchenko (2015), Tidal currents in the western Svalbard fjords, *Oceanologia*, *57*(4), 318–327.

Kuik, A., G. P. Van Vledder, and L. Holthuijsen (1988), A method for the routine analysis of pitch-and-roll buoy wave data, *J. Phys. Oceanogr.*, *18*(7), 1020–1034.

Langhorne, P. J., V. A. Squire, and C. Fox (1998), Break-up of sea ice by ocean waves, *Ann. Glaciol.*, *27*, 438–442.

Liu, A. K., and E. Mollo-Christensen (1988), Wave propagation in a solid ice pack, *J. Phys. Oceanogr.*, *18*(11), 1702–1712.

Long, R. B. (1980), The statistical evaluation of directional spectrum estimates derived from pitch/roll buoy data, *J. Phys. Oceanogr.*, *10*(6), 944–952.

Longuet-Higgins, M. S., D. Cartwright, and N. Smith (1963), Observations of the directional spectrum of sea waves using the motions of a floating buoy, in *Ocean Wave Spectra*, pp. 111–136, Prentice Hall, Englewood Cliffs, N. J.

Marsan, D., J. Weiss, E. Larose, and J.-P. Métaxian (2012), Sea-ice thickness measurement based on the dispersion of ice swell, *J. Acoust. Soc. Am.*, *131*(1), 80–91.

Meylan, M. H., L. G. Bennetts, and A. L. Kohout (2014), In situ measurements and analysis of ocean waves in the Antarctic marginal ice zone, *Geophys. Res. Lett.*, *41*, 5046–5051, doi:10.1002/2014GL060809.

Squire, V. (2007), Of ocean waves and sea-ice revisited, *Cold Reg. Sci. Technol.*, *49*(2), 110–133.

Squire, V. A., J. P. Dugan, P. Wadhams, P. J. Rottier, and A. K. Liu (1995), Of ocean waves and sea ice, *Annu. Rev. Fluid Mech.*, *27*(1), 115–168.

Thomson, J., and W. E. Rogers (2014), Swell and sea in the emerging arctic ocean, *Geophys. Res. Lett.*, *41*, 3136–3140, doi:10.1002/2014GL059983.

Tucker, M. J., and E. G. Pitt (2001), *Waves in Ocean Engineering*, vol. 5, 550 pp., Elsevier.

Wadhams, P. (1973), Attenuation of swell by sea ice, *J. Geophys. Res.*, *78*(18), 3552–3563.

Wang, R., and H. H. Shen (2010), Gravity waves propagating into an ice-covered ocean: A viscoelastic model, *J. Geophys. Res.*, *115*, C06024, doi:10.1029/2009JC005591.

Weber, J. E. (1987), Wave attenuation and wave drift in the marginal ice zone, *J. Phys. Oceanogr.*, *17*(12), 2351–2361.